

Multi-modal vision-language model for generalizable annotation-free pathology localization and clinical diagnosis

Hao Yang^{1,2,3†}, Hong-Yu Zhou^{5†}, Zhihuan Li⁶, Yuanxu Gao⁶, Cheng Li¹, Weijian Huang^{1,2,3}, Jiarun Liu^{1,2,3}, Hairong Zheng¹, Kang Zhang^{4,6*}, Shanshan Wang^{1,2*}

¹Paul C. Lauterbur Research Center for Biomedical Imaging, Shenzhen Institute of Advanced Technology, Chinese Academy of Sciences, Shenzhen, China.

²Peng Cheng Laboratory, Shenzhen, China.

³University of Chinese Academy of Sciences, Beijing, China.

⁴National Clinical Research Center for Ocular Diseases, Eye Hospital and Advanced Institute for Eye Health and Diseases, Wenzhou Medical University, Wenzhou, China.

⁵Department of Computer Science, The University of Hong Kong, Pokfulam, China.

⁶Institutute for Artificial Intelligence in Medicine and Faculty of Medicine, Macau University of Science and Technology, Macau, China.

*Corresponding author(s). E-mail(s): ss.wang@siat.ac.cn; kang.zhang@gmail.com;

†These authors contributed equally to this work.

Abstract

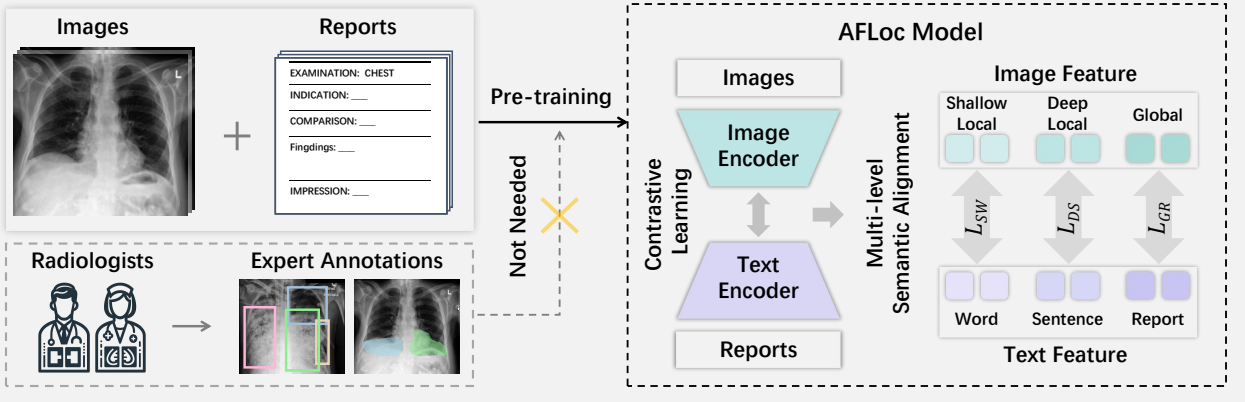
Defining pathologies automatically from medical images aids the understanding of the emergence and progression of diseases, and such an ability is crucial in clinical diagnostics. However, existing deep learning models heavily rely on expert annotations and lack generalization capabilities in open clinical environments. In this study, we present a generalizable vision-language model for Annotation-Free pathology Localization (AFLoc). The core strength of AFLoc lies in its extensive multi-level semantic structure-based contrastive learning, which comprehensively aligns multi-granularity medical concepts from reports with abundant image features, to adapt to the diverse expressions of pathologies and unseen pathologies without the reliance on image annotations from experts. We demonstrate the proof of concept on Chest X-ray images, with extensive experimental validation across 6 distinct external datasets, encompassing 13 types of chest pathologies. The results demonstrate that AFLoc surpasses state-of-the-art methods in pathology localization and classification, and even outperforms the human benchmark in locating 5 different pathologies. Additionally, we further verify its generalization ability by applying it to retinal fundus images. Our approach showcases AFLoc's versatility and underscores its suitability for clinical diagnosis in complex clinical environments.

Keywords: Annotation-Free Deep Learning, pathology localization, Vision-Language Pre-Training

Accurate diagnosis and precise pathology localization in medical images are paramount for optimizing treatment effectiveness and interventions. These technologies are instrumental in personalized medicine, facilitating customized treatment approaches that improve patient outcomes and mitigate the possibility of diagnostic errors. By pinpointing the exact location and extent of abnormalities, clinicians can make informed decisions that lead to more targeted therapies and improved prognoses for patients [1–4].

Over the past decade, supervised deep learning methods have significantly accelerated advancements in disease localization [5–8]. However, the efficacy of these methods heavily relies on extensively annotated training datasets, which require domain experts to invest considerable time [9]. Specifically, clinical localization tasks often require experienced clinicians to meticulously annotate numerous precise bounding boxes or perform pixel-wise delineations of localized pathology areas. This annotation process is costly, particularly in resource-constrained clinical settings, and algorithms frequently struggle to generalize to diverse datasets.

a. Annotation-free vision-language pre-training



b. Inference

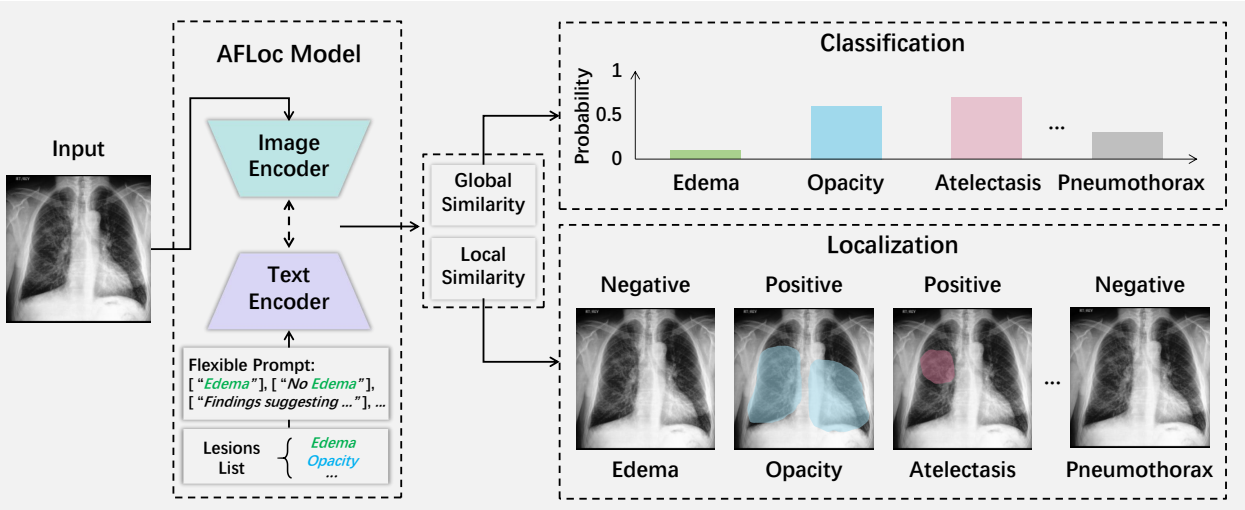


Fig. 1: Overview of the annotation-free pretraining and inference pipeline of the AFLoc model. a. Annotation-free vision-language pre-training: AFLoc leverages contrastive-based vision-language pre-training with existing images and text reports to eliminate the need for additional annotation efforts. A multi-level semantic alignment scheme is proposed to facilitate the comprehensive alignment of medical concepts across text reports with image features. b. Inference: AFLoc can classify and localize pathology within the prompt list. The model encodes the input image and the automatically generated text prompts into features. Feature similarity at local and global levels is used for diagnosis and localization. The image regions with positive findings are highlighted.

Several methods have been proposed to reduce the reliance on large annotated datasets [10–13]. Initially, these methodologies acquire general visual representations through self-supervised learning from image datasets, followed by fine-tuning on smaller annotated datasets. This approach enables models to achieve high performance on specific tasks while significantly decreasing the need and cost of data labeling [13]. Moreover, saliency-based methods [14–17] have been developed to reduce annotation costs in pathology localization tasks by allowing coarse localization of target categories in models trained with image-level annotations. However, these methods still require annotations for specific downstream tasks. This requirement is particularly challenging in flexible and dynamic clinical environments, especially for newly emerging diseases (e.g., COVID-19), where deployed models may fail to perform effectively [18–20].

In recent years, unsupervised deep learning methods have gained increasing attention due to their independence from annotated datasets, particularly in the field of anomaly detection [21–24]. These methods typically train models using only healthy samples, learning the distribution of normal anatomical structures, which enables the identification of abnormal pathology samples during the testing phase [21, 22]. They are particularly effective for data with simple structures and low inter-sample variance, allowing them to learn normative distributions and achieve excellent anomaly detection performance [23–25]. However, challenges such as the high heterogeneity of pathology images, significant similarities between different pathologies, and large variations in

contrast for the same lesions reduce the usability of these methods in complex scenarios, thereby hindering their practical application in real medical environments [25].

A promising approach is the development of medical visual-language pre-training methods [19, 26–31]. These methods establish effective correlations between medical reports and medical images, allowing them to flexibly localize disease types not encountered during pre-training without requiring additional customized annotations [19]. However, achieving precise pathology localization solely through the combination of medical images and clinical reports remains challenging. A primary obstacle is the lack of explicit pathology localization markers in clinical reports, which often provide only coarse information such as ‘upper’ or ‘left’ to indicate disease location. Moreover, clinical descriptions by clinicians are subjective and variable, further complicating the task of accurately extracting and localizing diseases in medical images. To address this challenge, several methods have been proposed to integrate finer-grained information. For instance, GLoRIA [30] extracts the correlation of the image’s regions and paired words in reports to learn global and local representations of images. MedKLIP [19] utilizes well-defined medical vocabulary knowledge bases to provide supervision at the entity level through triplet training paradigms. However, these fine-grained methods typically focus on individual levels of medical concepts and may overlook the variable meanings of concepts in different contexts. Therefore, these approaches may struggle to adapt to the diverse expressions of disease descriptors in clinical practice, often requiring customized textual cues to enhance localization performance.

In this study, we proposed AFLoc, a visual-language model based on contrastive learning aimed at alleviating the need for costly pathology localization annotations. AFLoc could autonomously perform pathology localization and clinical diagnosis in medical images. Unlike traditional global semantic alignment strategies [28, 29], AFLoc introduced a contrastive learning framework with a multi-level semantic alignment component, facilitating the comprehensive alignment of medical concepts from reports with image features. Specifically, the image encoder generated three levels of features: shallow local features, deep local features, and global features, which are aligned with word-level, sentence-level, and report-level features extracted by the text encoder. We validated AFLoc on two types of medical image datasets, including six external chest X-ray (CXR) datasets and a retinal fundus dataset. Our results demonstrated that AFLoc surpassed state-of-the-art methods in pathology localization and clinical diagnosis. Furthermore, AFLoc demonstrated robustness in handling unseen diseases, highlighting its adaptability to complex clinical environments.

Results

We used chest X-rays and retinal fundus datasets along with their corresponding clinical reports to train the model without the need for explicit annotations, as shown in Fig. 1. We evaluated our approach in two main aspects: pathology localization and diagnosis. We used the MIMIC-CXR dataset [32] to train our model, and subsequently evaluated it across six external datasets: RSNA Pneumonia [33], COVID Rural [34, 35], MS-CXR [28], CheXlocalize [14], ChestX-Det10 [36], and SIIM-ACR Pneumothorax [37]. For retinal fundus data, we collected 27,123 samples and conducted both diagnosis and localization tasks similar to the above chest X-ray experiments to verify the generalization of AFLoc on different medical modalities.

Our model is designed to support the automated diagnostic process, encompassing both pathology localization and classification. During the inference phase, doctors do not need to identify specific pathology labels; the model can directly classify the image and locate the pathology. Specifically, the model infers across all pathologies within a specified pathology scope, rather than relying on specific pathology keywords. In the experiment, the pathology scope includes all pathologies within the evaluation dataset. By traversing all pathologies, the method automatically generates text prompts to locate pathology and perform classification. This significantly reduces the workload of doctors and improves diagnostic efficiency.

Quantitative localization evaluation

Evaluation of localization performance was conducted using five external datasets. These datasets encompass 13 common thoracic pathologies: pneumonia, airspace opacity, atelectasis, cardiomegaly, consolidation, edema, enlarged cardiomeastinum, lung lesion, pleural effusion, pneumothorax, lung opacity, support devices, and COVID-19. Additionally, the datasets include three common retinal pathologies: choroidal neovascularization, drusen, and retinal hemorrhages. Accurate localization of these pathologies is critical for early diagnosis and treatment. For instance, in thoracic pathologies, airspace opacity can indicate lung infections, inflammation, or tumors [38]. Atelectasis leads to restricted gas exchange, causing hypoxemia and severely affecting respiratory function [39]. In retinal pathologies, detecting choroidal neovascularization is essential for the early diagnosis of wet age-related macular degeneration (AMD) [40]. Drusen are markers of dry AMD [40]. Retinal hemorrhages can indicate severe conditions such as diabetic retinopathy or hypertensive retinopathy [41]. Early detection and identification of these pathologies can significantly slow disease progression and enable preventive measures.

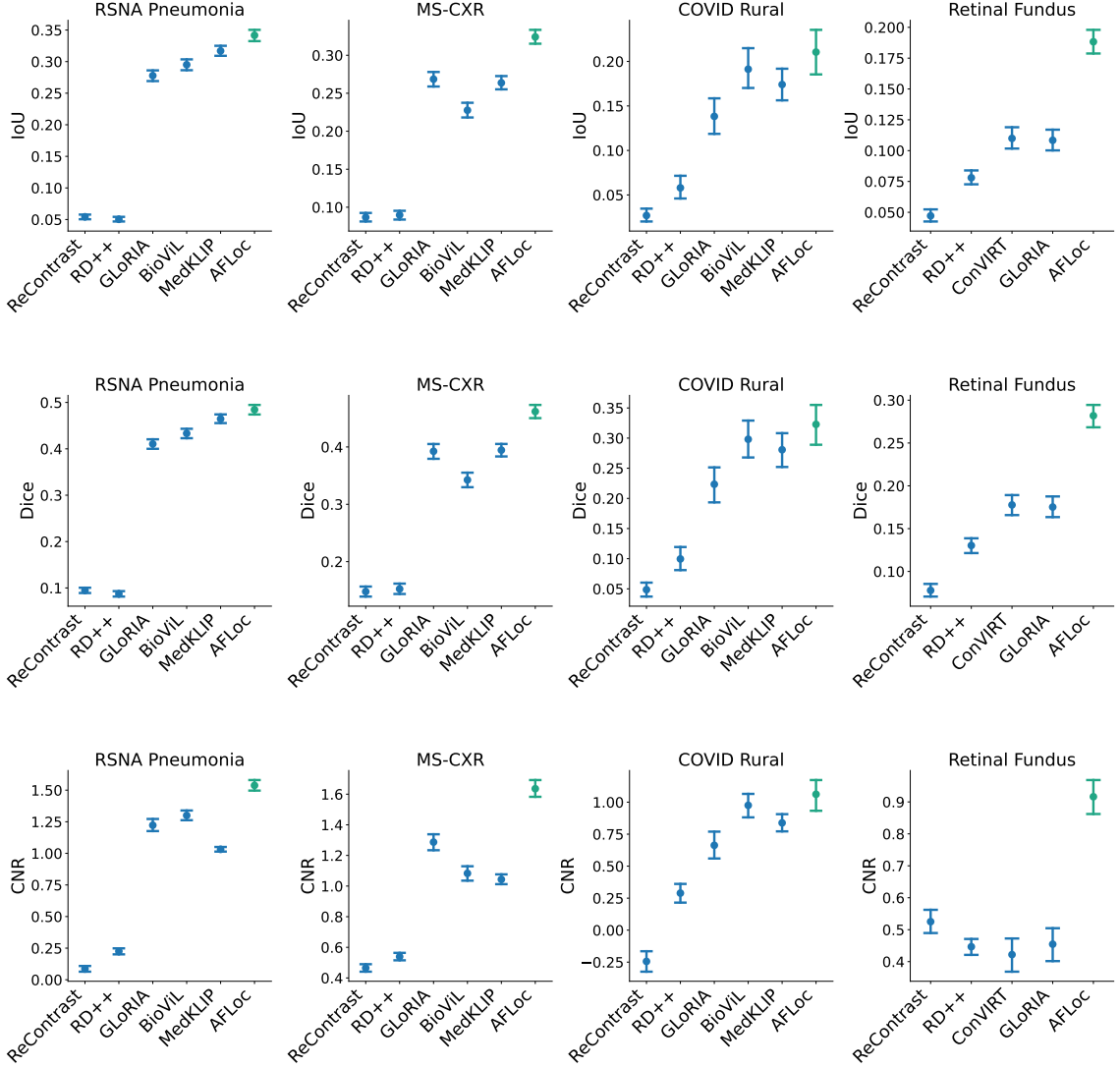


Fig. 2: Comparisons of AFLoc with state-of-the-art methods in the pathology localization task for chest X-ray and retinal fundus images. IoU, Dice similarity coefficient, and CNR with 95% CI on RSNA Pneumonia, MS-CXR, COVID Rural, and Retinal Fundus datasets are shown in the plots. Details in Extended Data Table 1 and Extended Data Table 4.

Here, we consider that ‘pathology localization’ encompasses both heatmap predictions and binary mask results. This distinction is crucial, as some clinical downstream applications may benefit more from the visualization provided by heatmaps rather than discrete segmentation. We evaluate each pathology heatmap using the Contrast-to-Noise Ratio (CNR) [28] and assess the thresholded segmentation masks using Intersection over Union (IoU) [42] and Dice similarity coefficient metrics.

For the RSNA Pneumonia, COVID Rural, MS-CXR, and retinal fundus datasets, the reported IoU and Dice were averaged over multiple threshold values: [0.1, 0.2, 0.3, 0.4, 0.5]. For the CheXlocalize dataset, we followed the methodology outlined in the reference literature [14] that determined an optimal threshold from the validation set and applied it to the test set. Additionally, we used the CNR [28] for measuring the difference between scores inside and outside the bounding box area, eliminating the need for a hard threshold. This assessment of local similarity is significant, as certain clinical downstream applications might benefit more from heatmap visualizations than discrete segmentation masks. To directly assess localization performance without the influence of classification errors, we reported localization performance on the positive slices of the dataset (those with ground truth segmentations or bounding boxes annotated by radiologists). This approach ensured that the evaluation focused on the accuracy of localization, without being confounded by classification errors [14]. The averages of these metrics are reported on the test set, based on over 1,000 bootstrap repetitions,

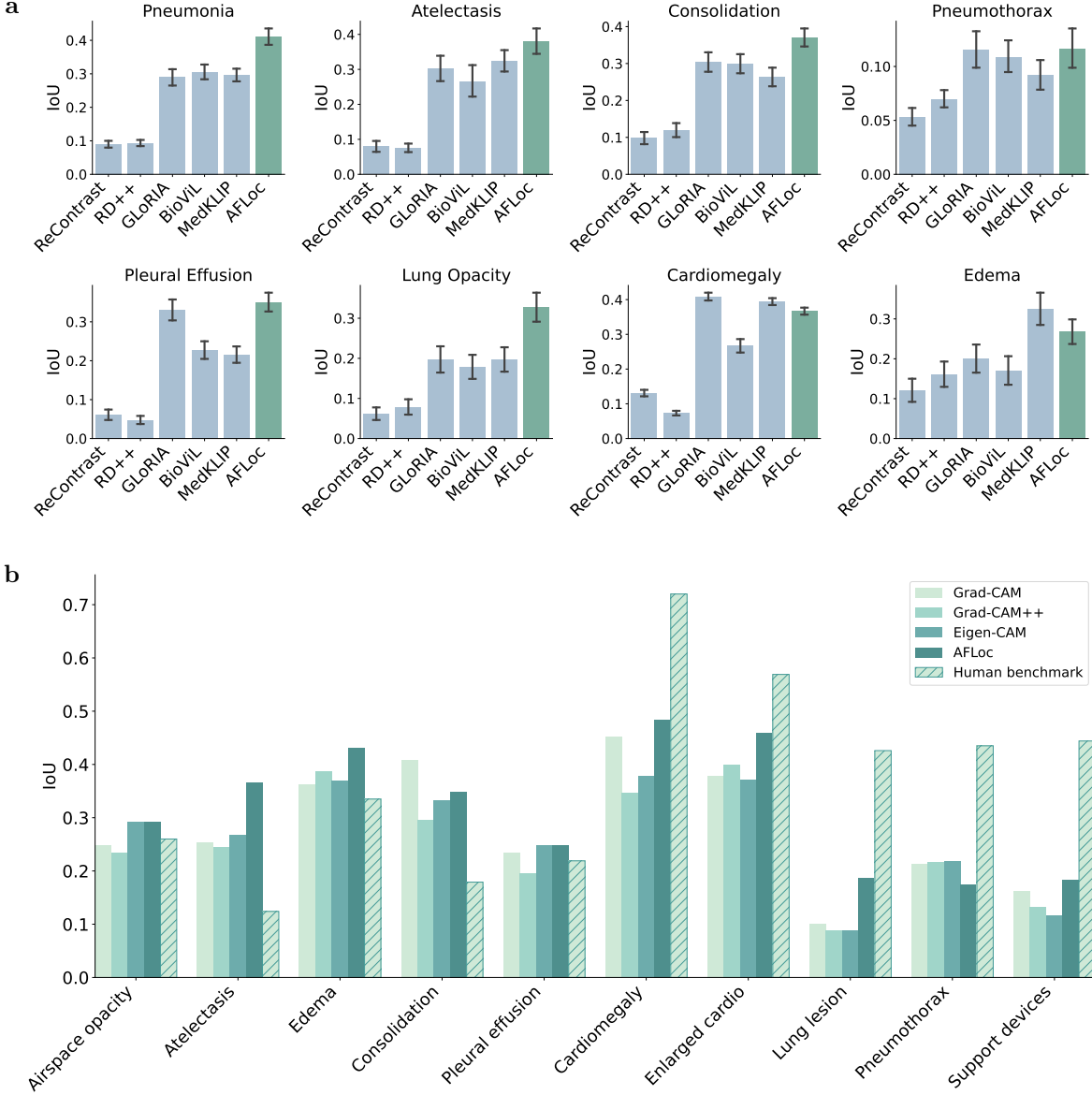


Fig. 3: Comparative evaluation of models for the localization of different chest pathologies. The bar graphs illustrate the mean IoU values for these models. Error bars represent the 95% CI. a. Results on the MS-CXR dataset. Comparisons of the proposed AFLoc with existing state-of-the-art unsupervised anomaly detection models and vision-language models. b. Results on the CheXlocalize dataset. Comparisons of the proposed AFLoc with various saliency methods and the human benchmark.

accompanied by the 95% confidence interval (CI), which was determined using the 2.5th and 97.5th percentiles of the empirical distribution.

RSNA Pneumonia. We reported the pneumonia localization results derived from the RSNA Pneumonia dataset. Diagnosing pneumonia accurately is a challenging task, requiring well-trained experts to review chest X-rays (CXR) and inspect various factors such as clinical history, vital signs, and laboratory exams. Pneumonia typically presents as one or multiple regions of increased opacity in CXR [43]. However, diagnosing pneumonia based on CXR can be complicated due to the presence of many other lung conditions, such as pulmonary edema, bleeding, atelectasis, lung cancer, or surgical changes. Additionally, pleural effusion outside the lungs can also appear as increased opacity in CXR. In this context, developing automated methods for pneumonia localization can be highly beneficial in the clinical environment.

The results are shown in Fig. 2. AFLoc outperforms all five comparative methods by a significant margin on three evaluation metrics. In terms of the IoU metric, AFLoc achieved 0.342 (95% CI: 0.332, 0.350), whereas GLoRIA, BioViL, and MedKLIP obtained 0.278 (95% CI: 0.269, 0.286), 0.295 (95% CI: 0.286, 0.304), and 0.317

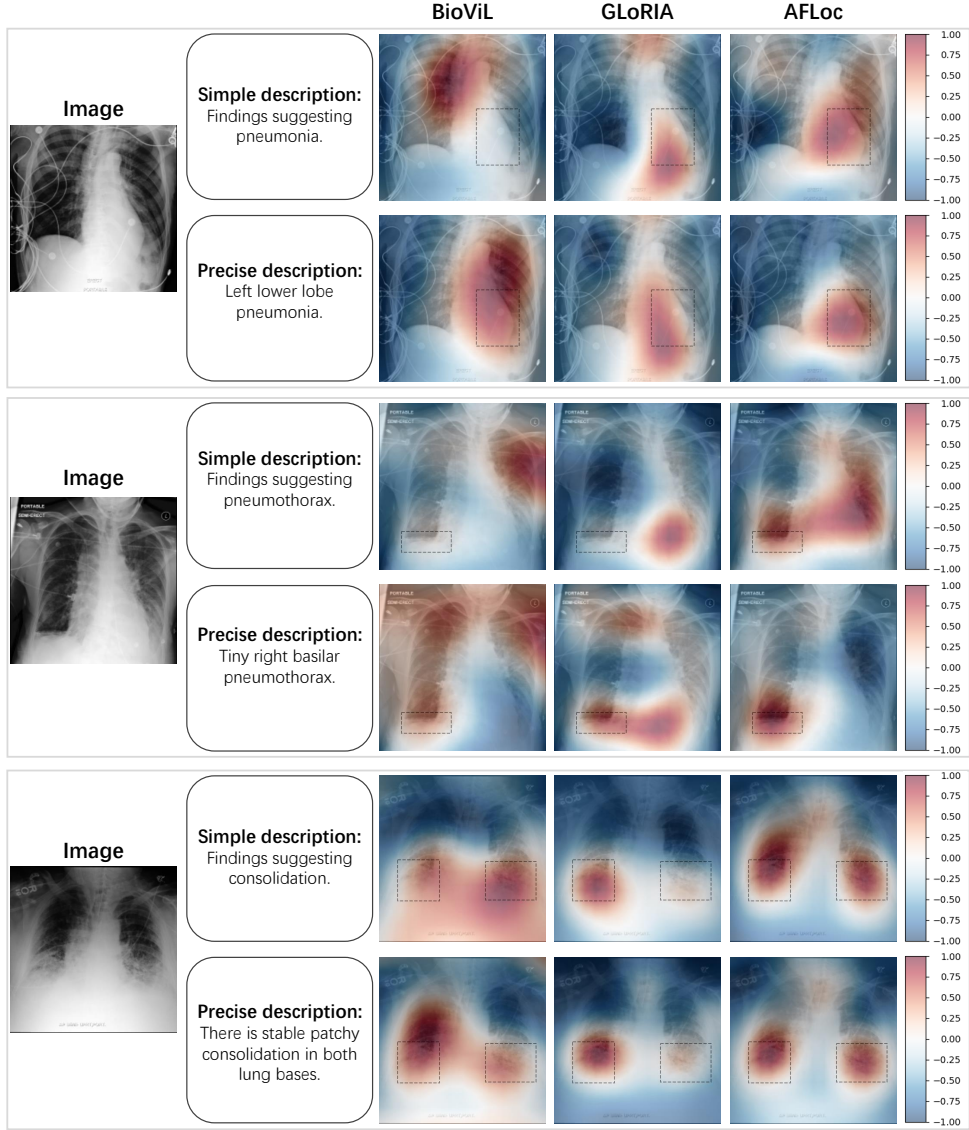


Fig. 4: Visualization of pathology localization by different models. Results with simple and precise descriptions are shown to demonstrate the models’ performance under different description granularities. Black dashed boxes indicate the pathology areas marked by radiologists, while deeper red indicates a higher focus level in the models’ predictions.

(95% CI: 0.309, 0.325), respectively. In terms of the Dice metric, AFLoc achieved 0.484 (95% CI: 0.474, 0.495), whereas GLoRIA, BioViL, and MedKLIP obtained 0.411 (95% CI: 0.400, 0.421), 0.433 (95% CI: 0.423, 0.443), and 0.465 (95% CI: 0.455, 0.474), respectively. In terms of the CNR metric, AFLoc achieved 1.538 (95% CI: 1.496, 1.580), whereas GLoRIA, BioViL, and MedKLIP obtained 1.223 (95% CI: 1.176, 1.272), 1.300 (95% CI: 1.262, 1.339), and 1.032 (95% CI: 1.014, 1.051), respectively. It is worth noting that on the RSNA Pneumonia datasets, AFLoc improved the IoU by 3% compared to the second-ranked algorithm. These results confirm that AFLoc can better localize pathology in CXR datasets compared to existing state-of-the-art methods.

MS-CXR. We performed the localization of cardiopulmonary radiological findings using the MS-CXR dataset. The MS-CXR dataset provides pathology-specific descriptions (precise descriptions), including bounding box annotation paired with radiological text descriptions. This dataset introduces a significantly more demanding real-world vision-language inference task compared to the RSNA Pneumonia dataset.

The results are plotted in the second column of Fig. 2. Detailed results can be found in Extended Data Table 1, Extended Data Table 2 and Extended Data Table 6. AFLoc demonstrated a significant advantage over GLoRIA, BioViL, and MedKLIP for the localization of cardiopulmonary radiological findings in CXR. Specifically, compared to GLoRIA (0.268; 95% CI: 0.242, 0.295), BioViL (0.228; 95% CI: 0.201, 0.255), and MedKLIP (0.264; 95% CI: 0.240, 0.288), our AFLoc (0.324; 95% CI: 0.298, 0.350) increased the IoU by more

Table 1: Quantitative results of different models on the MS-CXR dataset evaluated under two different descriptive scenarios. Numbers within parentheses indicate 95% CI.

Description	BioViL	GLoRIA	AFLoc
IoU			
Simple description	0.187 (0.162,0.213)	0.240 (0.214,0.265)	0.289 (0.262,0.314)
Precise description	0.228 (0.201,0.255)	0.268 (0.242,0.295)	0.324 (0.298,0.350)
Dice			
Simple description	0.287 (0.252,0.321)	0.357 (0.322,0.392)	0.418 (0.383,0.450)
Precise description	0.342 (0.308,0.377)	0.392 (0.357,0.427)	0.462 (0.431,0.492)
CNR			
Simple description	0.825 (0.694,0.948)	1.128 (1.003,1.254)	1.351 (1.219,1.481)
Precise description	1.083 (0.949,1.219)	1.287 (1.149,1.421)	1.636 (1.501,1.772)

than 6%, 7%, and 6%, respectively. Fig. 3a displays the results for specific pathologies. It can be observed that AFLoc showed significant improvements in lung opacity (11%), pneumonia (8%), atelectasis (6%), and consolidation (7%), demonstrating its superiority and generalization.

Additionally, two different descriptive scenarios were evaluated using the MS-CXR dataset: simple and precise descriptions. For instance, for pneumonia, the generated prompt is ‘Findings suggesting pneumonia’. The ‘precise description’ comes from the MS-CXR dataset, including phrases like ‘severe bibasilar consolidation’ and ‘air space opacity in a right infrahilar location’. Specifically, the sentences in this dataset come from medical reports written by physicians in real clinical environments. These sentences are customized and flexible, containing various clinical languages and terminologies that reflect actual medical practice. Since MedKLIP [19] employs a disease query mechanism, it is not applicable for this type of assessment.

AFLoc consistently outperformed comparison methods. Table 1 showed the quantitative results of pathology localization with different prompt qualities. Notably, when using simple descriptions only, AFLoc could still outperform comparison methods that use precise descriptions. As shown in Fig. 4, AFLoc could accurately locate the pathology regions, no matter whether using a well-designed high-quality prompt or a simple automatically generated prompt. Nevertheless, it should be noted that improving the quality of the text prompts helped to refine the localization results. A better description helped to delineate the fine-grained boundaries and remove irrelevant low-confidence artifacts. These results indicated that AFLoc not only achieved better performance with simple descriptions but also supported customized statements, making it more suitable for clinical practice.

CheXlocalize. We evaluated our method in a larger scope. In addition to comparing with the aforementioned vision-language pre-training models, we also compared AFLoc with three state-of-the-art saliency-based methods on the CheXlocalize dataset: Grad-CAM [15], Grad-CAM++ [16], and Eigen-CAM [17]. We included a human benchmark [14] to assess performance levels. These saliency methods are trained under fixed categories and require image-level labels [14]. They generate heatmaps that highlight the medical image regions most influential for deep neural network (DNN) predictions. Saliency methods are particularly useful in medical image analysis as they provide model explainability, generating heatmaps without requiring bounding box annotations or pixel-level segmentation during training.

Our method was directly compared with the published results of CheXlocalize, as shown in Fig. 3b and Extended Data Table 5. Notably, AFLoc outperformed the saliency methods in most cases, despite not relying on image-level or location-level annotations, which are required by the saliency methods. AFLoc showed significant performance improvements in localizing specific pathologies such as atelectasis (10%), lung lesions (9%), enlarged cardiomedastinum (6%), and edema (4%). The average IoU (0.318) achieved by AFLoc was about 4% higher than that of the best comparison method, Grad-CAM (0.282). Additionally, AFLoc surpassed the human benchmark in localizing five different pathologies (airspace opacity, atelectasis, edema, consolidation, and pleural effusion). These findings highlighted the potential of AFLoc in the field of medical image analysis.

COVID Rural. The capability of a model to generalize to unseen diseases is significant in clinical applications. To assess this generalization ability, we evaluated different models (GLoRIA, BioViL, MedKLIP, and the proposed AFLoc) using the COVID Rural dataset, which had been collected for COVID-19 detection. As all the models were trained on the dataset, which had been collected before the emergence of COVID-19 and lacks

information about the virus, their performance on the COVID Rural dataset can serve as a means to evaluate their capability to generalize to unseen diseases.

The quantitative results were plotted in Fig. 2 and listed in Extended Data Table 1. AFLoc (IoU: 0.211; 95%CI: 0.185, 0.236. Dice: 0.323; 95%CI: 0.289, 0.355. CNR: 1.062; 95%CI: 0.929, 1.173) achieved superior performance compared to GLoRIA’s (IoU: 0.138; 95%CI: 0.119, 0.159. Dice: 0.223; 95%CI: 0.193, 0.251. CNR: 0.663; 95%CI: 0.560, 0.770), BioViL’s (IoU: 0.191, 95%CI: 0.170, 0.215. Dice: 0.298; 95%CI: 0.268, 0.329. CNR: 0.975; 95%CI: 0.880, 1.065), and MedKLIP’s (IoU: 0.174; 95%CI: 0.156, 0.192. Dice: 0.281; 95%CI: 0.252, 0.308. CNR: 0.838; 95%CI: 0.772, 0.906) in terms of both IoU and CNR metrics. These results indicated that AFLoc could better generalize to unseen diseases, which could be a valuable characteristic when applied in clinical situations.

Retinal Fundus. To further demonstrate the generalizability of our method, we applied it to retinal fundus images. Column 4 of Fig. 2 showed the localization results on the retinal fundus dataset. The localization performance for three types of retinal pathologies was detailed in Extended Data Table 4. The two unsupervised anomaly detection methods showed higher confidence in pathology areas, as indicated by the CNR metric, compared to the vision-language method. However, their IoU and Dice were lower than those of the vision-language method. This suggests that while the unsupervised methods had higher confidence within the pathology areas and less noise outside these regions, the vision-language method benefited from hard thresholding. Our approach consistently outperformed all methods across all three metrics, demonstrating its exceptional capability in pathology localization.

Quantitative diagnosis evaluation

In this section, we presented the diagnostic performance of AFLoc through zero-shot classification. Both CXR and retinal fundus datasets were utilized. Notably, two unsupervised anomaly detection methods were also compared, as these methods had not encountered the downstream disease types either, for convenience, we used the term ‘zero-shot’ to describe them. We used the area under the receiver characteristic operating curve (AUROC) to evaluate the model’s classification performance, reflecting the overall classification capability across different thresholds.

Table 2: Comparison of AUROC on RSNA and SIIM datasets for the zero-shot classification task.

Methods	RSNA Pneumonia	SIIM
ReContrast	0.632	0.578
RD++	0.566	0.507
ConVIRT	0.804	0.643
GLoRIA	0.715	0.534
BioViL	0.828	0.708
CheXzero	0.858	0.688
MedKLIP	0.869	0.892
AFLoc	0.892	0.896

We performed zero-shot classification tasks on the RSNA and SIMM CXR datasets. As shown in Table 2, the two saliency-based methods (ReContrast and RD++) scored lower compared to vision-language multi-modal pre-training methods. This underscored the importance of expert-knowledge-rich text reports. MedKLIP performed well in this task, likely because of its unique semantic simplification of text reports, which enabled the model to learn classification-relevant knowledge extensively. AFLoc achieved AUROC scores of 89.2% and 89.6% on the two datasets, respectively, demonstrating that the proposed multi-modal semantic alignment method effectively captures the classification features from both text and images.

To further demonstrate the generalizability of our method, we also applied it to retinal fundus images. Table 3 presented the corresponding results, detailing scores for nine types of retinal diseases to ensure a fair comparison. These nine diseases include Macular Degeneration (MD), Retinopathy, Myopia, Glaucoma, Congenital Optic Disc Anomalies (CODA), Retinal Arteriosclerosis (RAS), Cataract, Macular Epiretinal Membrane (MEM), and Macular Lesion (ML). In this comparison, two unsupervised anomaly detection methods achieved high performance in certain specific diseases, with ReContrast scoring 0.921 AUROC for Myopia and RD++ scoring 0.819 AUROC for Cataract. However, their average scores lagged behind the vision-language pre-training methods, at 0.589 and 0.52, respectively. Impressively, AFLoc achieved the highest scores across all nine types of retinal diseases, with an average AUROC of 0.908, significantly surpassing the second-best method, GLoRIA, which scored 0.772. We also compared AFLoc with RETFound, a method that used labeled fine-tuning, and

found that AFLoc achieved comparable performance. Overall, AFLoc not only proved effective on the CXR dataset but also achieved the highest performance on the retinal fundus dataset, demonstrating its exceptional diagnostic capability and disease generalization potential.

Table 3: Comparison of AUROC on retinal fundus datasets for the zero-shot classification task. RETFound utilizes human-annotated classification labels during fine-tuning.

Methods	Label free	MD	Retinopathy	Myopia	Glaucoma	CODA	RAS	Cataract	MEM	ML	Mean
ReContrast	✓	0.423	0.689	0.921	0.693	0.468	0.408	0.341	0.546	0.812	0.589
RD++	✓	0.569	0.518	0.291	0.431	0.634	0.671	0.819	0.569	0.176	0.520
ConVIRT	✓	0.421	0.759	0.870	0.848	0.854	0.466	0.424	0.862	0.698	0.689
GLoRIA	✓	0.914	0.592	0.774	0.926	0.803	0.636	0.610	0.834	0.864	0.772
AFLoc	✓	0.978	0.839	0.962	0.938	0.899	0.643	0.987	0.978	0.946	0.908
RETFound	✗	0.935	0.758	0.971	0.918	0.900	0.901	0.995	0.908	0.883	0.908

Qualitative visualization

To intuitively demonstrate the localization performance of our method, we presented heatmap visualization in Fig. 5. Both Chest X-ray and retinal fundus images with various pathologies types were considered. Here, the intensity of the red regions indicated the probability that the model predicted these areas as diseased, while the black boxes represented the gold standard annotated by clinicians.

In Fig. 5a, we illustrated AFLoc’s ability to identify multiple pathologies in X-ray images. As different text inputs were applied to a single case (image), the model still demonstrated robust heatmap results for those pathologies. Notably, AFLoc could accurately identify small lesions, such as Effusion in the second row, proving its capability in detecting both multiple and minute lesions.

In Fig. 5b, we applied AFLoc to retinal fundus images, mainly showcasing the localization performance for choroidal neovascularization, drusen, and retinal hemorrhages. For choroidal neovascularization and drusen, the pathology areas were relatively concentrated, and AFLoc accurately localized these pathologies. Conversely, in cases of retinal hemorrhages, the lesions appeared as scattered and minute regions, posing a significant challenge for automatic localization. Despite not being able to perfectly localize every hemorrhage spot, AFLoc’s heatmaps still highlight some major hemorrhage areas.

Ablation Study

In the ablation study, we explored the impact of using word-level, sentence-level, and report-level text features on the performance of AFLoc. The results are listed in Extended Data Table 3. When using only one level of text features, the performance of AFLoc deteriorates a lot, especially for word-level and report-level features. One possible explanation could be that the word-level features lack sufficient contextual information to capture the characteristics of the pathology, whereas the report-level features may fail to capture critical diagnostic details due to their overly macroscopic perspective. On the other hand, AFLoc using sentence-level features achieves relatively higher performance, suggesting that sentence-level features can provide richer contextual information, which is important for pathology localization in medical imaging. When these different levels of text features were combined in utilization, clear performance enhancement could be observed, and the best performance was achieved when all three levels were employed, fully supporting our hypothesis that the combination of multi-level information is crucial for improving the accuracy of pathology localization in medical images.

Text encoders play a crucial role in deeply understanding medical concepts and achieving superior semantic alignment. To study the impact of text encoding on performance, we introduced the text encoder from the latest large language and vision assistant for biomedicine (LLaVA-Med [44]). LLaVA-Med had shown improvements in open biomedical question-answering tasks. However, as demonstrated in Extended Data Table 7, its performance still fell short of BioClinicalBERT [45]. This discrepancy could be attributed to the superior performance of language models trained on domain-specific (e.g., biomedical and clinical) datasets for their respective domain tasks [46]. LLaVA-Med was trained on the PMC-15M dataset, which is extracted from scientific publications in PubMed Central, whereas BioClinicalBERT was trained on electronic health records of intensive care unit patients, aligning more closely with the clinical diagnosis reports used in this study.

Discussion

Pathology localization and diagnosis are crucial for clinical applications in medical imaging. However, existing methods faced significant challenges related to limited annotated data and generalization capability [18, 19].

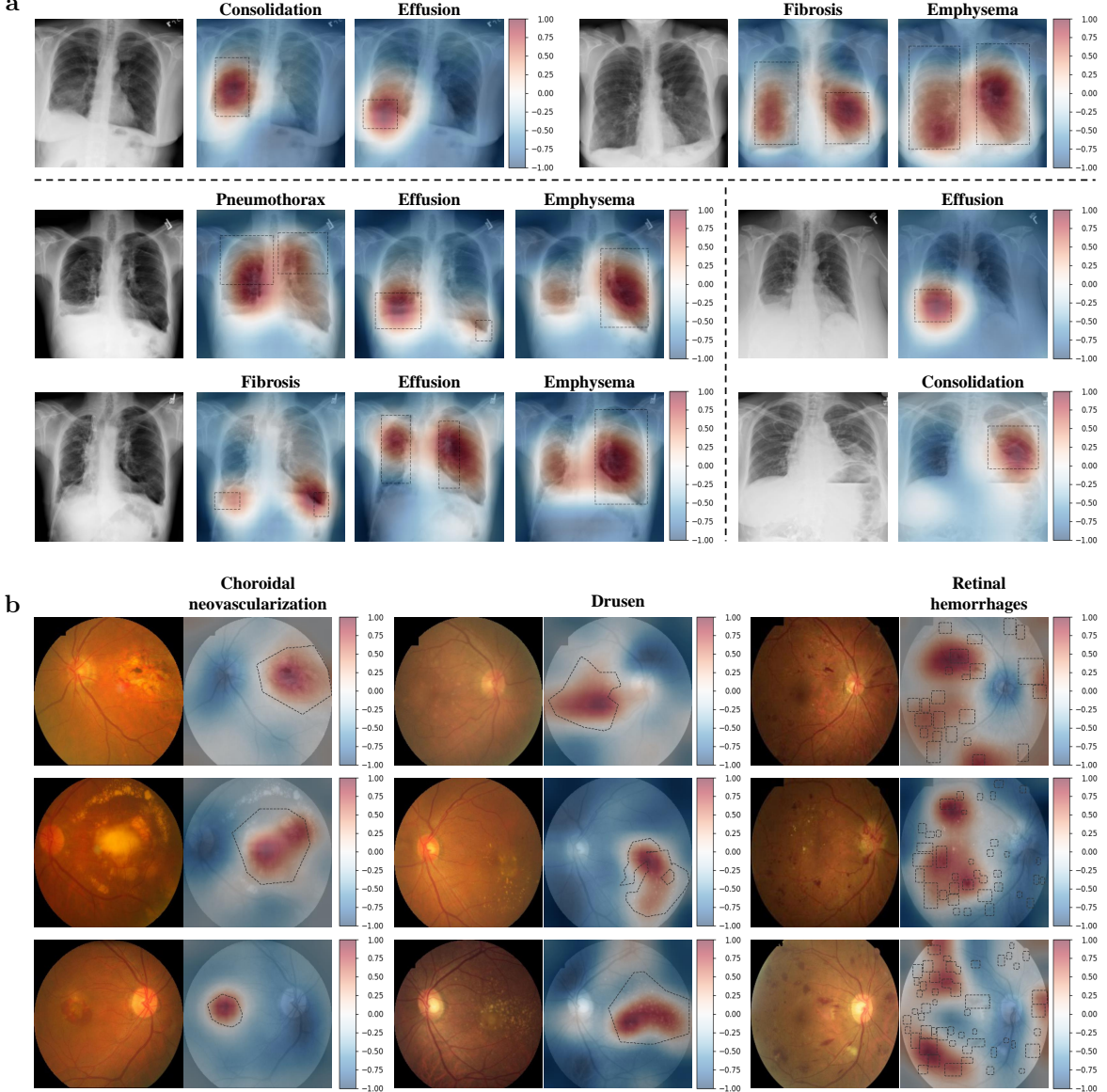


Fig. 5: Visualization of multiple pathologies and multiple datasets. a. Chest X-ray (ChestX-Det10). b. Retinal fundus images with various pathology types are considered. Black dashed boxes indicate the pathology areas marked by radiologists, and the intensity of red in the heatmaps signifies the focus level of the model’s prediction, with deeper red indicating higher focus.

In this paper, we introduced AFLoc, an annotation-free deep learning model designed to generalize pathology localization through pre-training with both clinical reports and imaging data.

Unlike existing pre-trained vision-language models that rely solely on global information for contrastive learning [28], AFLoc employed a multi-level semantic alignment approach to achieve refined medical feature representation. The rationale behind our design was that pathology often occupies only a small part of the entire image, making global information-based models insufficient for accurate localization. While some methods incorporated both global and local text-image feature alignment [30], they typically used words as alignment units, which might have overlooked the complete semantic information of sentences. However, pathologies were often described in sentences that contained comprehensive and detailed localizing information. In contrast, AFLoc made full use of semantic information by utilizing word-level, sentence-level, and report-level text features during pre-training, capturing the nuanced information crucial for accurate pathology localization.

The localization of pathology such as pneumonia and effusion in CXR is crucial for clinicians, significantly enhancing diagnostic accuracy and informing treatment decisions. We evaluated AFLoc using four open-source datasets: RSNA Pneumonia, MS-CXR, CheXlocalize, and COVID Rural, comparing it with several advanced

methods. In the RSNA dataset, AFLoc demonstrated superior performance in localizing pneumonia, outperforming five other methods (Fig. 2 and Fig. 3). This validated the effectiveness of our proposed multi-level semantic alignment strategy for chest pathology localization. In the MS-CXR dataset, we evaluated AFLoc’s robustness to unstructured prompts. We compared the localization results of simple descriptions and clinically enhanced precise descriptions as text inputs. It was observed that precise descriptions outperformed simple descriptions and also surpassed the two state-of-the-art vision-language methods, GLoRIA and BioViL. This demonstrated the robustness of our method in handling unstructured text inputs, thereby enabling clinicians to interact seamlessly with the model. We conducted multi-pathology localization on the CheXlocalize dataset and compared the results with human annotators. Excitingly, our method exceeded the human baseline in five tasks, highlighting AFLoc’s potential for clinical deployment. To further demonstrate AFLoc’s robustness against unseen diseases, we evaluated it on the COVID Rural dataset. AFLoc again achieved the highest localization results for COVID-19, showcasing its capability to identify unknown diseases, which is crucial in the complex and dynamic clinical environment. Finally, to prove the generalizability of AFLoc, we retrained the model on the retinal fundus image dataset and performed a similar evaluation process. The results indicated that AFLoc not only performed well on the CXR dataset but also achieved top-level performance on fundus data, thus confirming the proposed model’s versatility.

The significant advantage of AFLoc in localizing unseen pathologies (i.e., COVID-19) as demonstrated when evaluated on the COVID Rural dataset could be attributed to two key factors. First, the symptoms of COVID-19 in X-ray images, such as patchy shadows in the lungs, interstitial changes, and ground-glass opacities, were not unique to COVID-19 and can usually be observed in non-COVID-19 pneumonia cases as well. Therefore, although the utilized training dataset, MIMIC-CXR, lacked information about the COVID-19 virus, AFLoc could learn relevant pathology knowledge from the diagnostic reports and effectively apply it to diagnose this unseen disease. During the inference phase, related pathology descriptions were used to identify this unseen disease. Second, compared to existing methods that simply match original reports with image scans or use domain knowledge-enhanced approaches, AFLoc is more advanced and detailed. It focused on mining the hierarchical information in images and reports and implicitly learned the complex relationships between different levels of features. Through this design, AFLoc could deeply understand and differentiate the subtle differences between various radiological findings, thereby achieving higher accuracy and effectiveness in the localization of unseen pathologies.

In addition to its localization capabilities, we also demonstrated AFLoc’s diagnostic performance to expand its applicability in clinical practice. As previously mentioned, we conducted experiments on both CXR and retinal fundus datasets (Table 2 and Table 3). The experimental results showed that AFLoc achieved superior diagnostic performance compared to existing methods that do not require classification annotations. Moreover, we found that AFLoc performed comparable performance to RETFound which utilized annotated data. This is likely because our method effectively extracted valuable semantic knowledge from clinical reports through sentence-level semantic alignment, thereby reducing the need for labor-intensive image annotations during training.

Lastly, we qualitatively presented the visual localization results for both CXR and retinal fundus data (Fig. 5). In the Chest X-Det10 dataset, we demonstrated AFLoc’s robustness in handling multiple areas of a single pathology and multiple pathologies in a single case. We believe this aligns well with real-world clinical scenarios and further validates AFLoc’s high performance in these complex situations. Additionally, we showcased the results on the retinal fundus dataset, focusing on three types of pathologies: choroidal neovascularization, drusen, and retinal hemorrhages. AFLoc performed well in the first two pathologies but showed room for improvement in areas involving numerous small retinal hemorrhages.

Overall, extensive experiments have demonstrated that AFLoc achieved superior performance in pathology localization and diagnosis across multiple datasets, even surpassing human benchmarks in five pathologies tasks (airspace opacity, atelectasis, edema, consolidation, and pleural effusion). AFLoc not only possessed automatic diagnostic and localization capabilities but also supported free-form description input for enhanced performance. It outperformed state-of-the-art methods on both CXR and retinal fundus datasets, indicating its versatility. The performance improvements of AFLoc could be attributed to its innovative design, which incorporates a multi-level semantic component. This design effectively established robust correlations between complex medical concepts (text) and images of various granularities without requiring additional annotations. This capability significantly enhances pathology localization.

Despite all these clinically valuable characteristics, AFLoc has some limitations. Firstly, although AFLoc had outperformed existing medical vision-language methods, saliency methods, and unsupervised anomaly localization methods in pathology localization, there is still room for improvement in achieving precise pathology segmentation. Exploring more sophisticated image feature extraction approaches, such as better aligning local features of proposal regions generated by multi-scale anchor boxes with text features, may further improve model performance. Additionally, there are viable alternatives when annotations are available [47]. Secondly,

the training dataset we used was relatively small, especially compared to those available in the natural image domain. With larger training datasets, the performance of AFLoc could be further enhanced. Furthermore, this study involved two modalities: chest X-rays and retinal fundus. To further validate its broad applicability, we planned to extend our experiments to other medical imaging modalities or organs in the future and present our findings accordingly. Finally, the current model could not correct possible errors in the provided text prompts or offer more detailed pathology descriptions and etiological analyses. In the future, we plan to explore these directions to make AFLoc more effective and comprehensive.

In summary, we have developed an annotation-free vision-language model, AFLoc, that could generalize well to locate and diagnose various pathologies in both chest X-rays and retinal fundus images provided by corresponding pathologies text descriptions. Extensive experimental results showed that AFLoc could outperform existing state-of-the-art medical vision-language methods, saliency methods, and unsupervised anomaly detection methods, highlighting its immense potential in real-world clinical applications where a large amount of unannotated data exists.

Methods

Dataset

In our chest X-ray experiments, we utilized the MIMIC-CXR dataset for training. We then evaluated the model across six external datasets: RSNA, MS-CXR, CheXlocalize, COVID Rural, SIIM-ACR Pneumothorax, and ChestX-Det10. Additionally, to validate the model’s adaptability to different modalities, we collected retinal fundus data. For the retinal fundus experiments, the model was retrained using image-report pairs from this dataset.

MIMIC-CXR [32]. The MIMIC-CXR dataset is an extensive, publicly available collection of chest X-ray images, paired with free-text radiological reports. It contains 377,110 images that are linked to 227,835 radiological studies. Each study within the database may consist of one or more images, providing a diverse range of scanning perspectives for analysis and research purposes.

RSNA Pneumonia [33]. The RSNA Pneumonia dataset presents a challenge in identifying visual signals of pneumonia from medical images. Images in this dataset are accompanied by bounding box labels that indicate the areas affected by pneumonia. Over 1000 cases in this dataset are positive, with each image potentially containing one or more boundary boxes highlighting the pneumonia regions.

MS-CXR [28]. MS-CXR is a curated database that features 1,153 image-sentence pairs of bounding boxes along with their corresponding phrases. This collection encompasses 8 different types of cardiopulmonary radiological findings. The image-sentence pairs are distributed equally among the 8 findings. In addition to brief descriptions, this dataset provides authentic depictions of radiological findings as described in radiology reports and oral records. All the data have been annotated and validated by professional radiologists, ensuring a gold standard for phrase grounding assessment. MS-CXR is a subset of the MIMIC-CXR dataset. All data in MS-CXR have been removed from the MIMIC-CXR training set to ensure it was not used in the training process.

CheXlocalize [14]. The CheXlocalize dataset is a comprehensively curated chest X-ray dataset. It features multi-label, pixel-level segmentations meticulously drawn by two board-certified radiologists, ensuring a highly precise ground truth annotation for each image. This dataset includes 234 images, encompassing 643 segmented pathologies. It covers a broad range of cardiopulmonary conditions, including airspace opacity, atelectasis, cardiomegaly, consolidation, edema, enlarged cardiomedastinum, lung lesion, pleural effusion, pneumothorax, and support devices. Moreover, CheXlocalize also provides human benchmark segmentations, drawn by a separate group of 3 board-certified radiologists, which can be used to study human benchmark localization performance.

COVID Rural [34, 35]. The COVID Rural project includes 221 chest X-ray images from 105 patients who tested positive for COVID-19. In these images, opaque areas associated with COVID-19 infection are delineated by polygons that connect specific points. The manual annotations of these images were generated by primary physicians and reviewed by experienced radiologists.

SIIM-ACR Pneumothorax (SIIM) [37]. The SIIM dataset is designed to promote the development of models for identifying pneumothorax. It includes more than 120,000 frontal chest X-rays, each of which has been precisely annotated. Employing the data partitioning method described by [30], we conducted tests on the test set.

ChestX-Det10 is a subset of the NIH ChestXray14 dataset, consisting of 3,543 chest X-ray images. These images have been annotated with bounding boxes for 10 diseases/abnormalities by three board-certified radiologists. In this study, we followed the official data splits and conducted qualitative visual evaluations of our model on the test set.

Retinal Fundus. This dataset was compiled from a total of 26,028 retinal fundus images and paired reports from 11,372 individuals. All fundus images were captured using a Zeiss fundus camera and annotated by retinal

experts with 10 years of experience for nine common retinal diseases. We divided the data set into training, validation, and testing sets by 8:1:1 based on the patient’s unique ID, which ensures that the same patient does not appear in the same data set. Our model was trained and validated on the training and validation sets, respectively, and classification performance evaluations were done on the testing dataset. To evaluate the performance of our model in pathology localization, we utilized an additional dataset for validation, which was annotated at the pixel level by retinal specialists. Specifically, this dataset includes 437 images of Choroidal neovascularization, 160 images of drusen, and 498 images of retinal hemorrhage.

Approvals for the research were secured from the Institutional Review Board/Ethics Committees of all participating hospitals or institutes. Consent forms were signed by all involved patients. The study was carried out in accordance with the United States Health Insurance Portability and Accountability Act. Furthermore, it was in compliance with the principles of the Declaration of Helsinki, and conformed to policies of the Chinese Center for Disease Control and Prevention, as well as the Chinese Health Laws.

The Proposed AFLoc Model

Text encoding. The original radiology reports usually include a ‘Findings’ section, detailing clinical observations, and an ‘Impressions’ section. These sections typically contain multiple sentences. In GLoRIA [30], a block tokenization technique was used, constructing complete words by aggregating multiple subwords. On the other hand, BioViL [28] employs a custom dictionary developed from multiple datasets, aiming to reduce the frequency of words being split into subwords. A radiological finding in an image might require information of location, size, and severity for a comprehensive description. Treating words as independent entities may overlook the complete semantics, leading to incorrect semantic alignment between text and image. In our proposed AFLoc, text features are extracted at three levels: word-level, sentence-level, and report-level, aiming to represent report content more comprehensively and precisely through multi-granularity semantics. Additionally, this three levels structure is naturally present in the text, requiring no complex designs to accomplish our text encoding.

Specifically, we employ BioClinicalBERT [45] as our text encoder to extract text features. When processing a medical report x_t containing Q words and P sentences, each word is tokenized into q_i tokens. The tokenizer inputs the tokenized report into the text encoder $e_t^I \in \mathbb{R}^H$, where H is the maximum token length. The text encoder outputs $e_t^O \in \mathbb{R}^{L \times H \times D}$, L is the number of layers, and D indicates the feature dimension. We take the average feature of the last 4 layers as the subword-level feature $t_{sub} \in \mathbb{R}^{H \times D}$. Then, we aggregate features at the word, sentence, and report levels. Particularly, for a word, all its subword-level features are summarized to obtain Q the word-level features t_w . On the other hand, all corresponding subword-level features are averaged to obtain P sentence-level features t_s and one report-level feature t_r .

Image encoding. We adopt a popular architecture, ResNet-50 [48], as the backbone of our image encoder E_v . When processing the input image x_v , we extract image features from specific intermediate convolutional layers from the image encoder. Shallow features are extracted from the third down-sampling stage, and deep features are from the fourth down-sampling stage. Additionally, the features from the last convolutional layer of ResNet-50 are average pooled to obtain the global image features. Then, we use two 1×1 convolutions and a linear layer to adjust the dimensions of the three different levels of image features to match the text feature dimensions. We obtain shallow local features $v_s \in \mathbb{R}^{D \times M}$, deep local features $v_d \in \mathbb{R}^{D \times \frac{M}{4}}$, and global features $v_g \in \mathbb{R}^D$, where M denotes the number of sub-regions in shallow features, and D represents the feature dimension.

Multi-level semantic alignment. Given that medical reports usually provide detailed descriptions corresponding to the observations in medical images, the images and their corresponding reports should exhibit consistent semantic properties in the multimodal feature space. This inspires us to perform semantic alignment between image features and text features at the three levels of different granularities. Specifically, shallow and deep image features extracted by the image encoder are aligned with the word-level and sentence-level text features extracted by the text encoder for local semantic alignment, while the global image features and the report-level text features are aligned for global semantic alignment. The detailed process is depicted in Fig. 1.

For local semantic alignment, we adopt the localized feature matching function $Z(\cdot, \cdot)$ [30]. Taking sentence features as an example, the similarity matrix between P sentences and $M/4$ image sub-regions is represented as:

$$s = v_d^T t_s \quad (1)$$

The image feature representation, weighted by sentences c_i and localized feature matching function $Z(\cdot, \cdot)$ are represented as:

$$c_i = \sum_{j=1}^{\frac{M}{4}} \log \frac{\exp(s_{ij})/\tau_1}{\sum_{k=1}^{\frac{M}{4}} \exp(s_{ik})/\tau_1} v_{dj} \quad (2)$$

$$Z(c, t) = \log \left(\sum_{i=1}^N \exp(\Phi(c_i, t_i)/\tau_2) \right) \quad (3)$$

τ_1 and τ_2 are scaling factors, and N represents the size of the first dimension of the local features (i.e., P for sentence-level features). $\Phi(c_i, t_i)$ is used to calculate the cosine similarity between the two vectors (c_i, t_i) . The local contrastive loss between deep features and sentence-level features is defined as:

$$L_{DS} = -\frac{1}{B} \sum_i^B \left(\log \frac{\exp(Z(v_d^i, t_s^i)/\tau_3)}{\sum_{k=1}^B \exp(Z(v_d^i, t_s^k)/\tau_3)} + \log \frac{\exp(Z(v_d^i, t_s^i)/\tau_3)}{\sum_{k=1}^B \exp(Z(v_d^k, t_s^i)/\tau_3)} \right) \quad (4)$$

where τ_3 is a temperature parameter and B is the batch size. Similarly, we obtain the contrastive loss between shallow features and word-level features:

$$L_{SW} = -\frac{1}{B} \sum_i^B \left(\log \frac{\exp(Z(v_s^i, t_w^i)/\tau_3)}{\sum_{k=1}^B \exp(Z(v_s^i, t_w^k)/\tau_3)} + \log \frac{\exp(Z(v_s^i, t_w^i)/\tau_3)}{\sum_{k=1}^B \exp(Z(v_s^k, t_w^i)/\tau_3)} \right) \quad (5)$$

For global semantic alignment, we optimize the global features and report-level features by using paired and unpaired samples of images and texts according to the following loss function:

$$L_{GR} = -\frac{1}{B} \sum_i^B \left(\log \frac{\exp(\Phi(v_g^i, t_r^i)/\tau_3)}{\sum_{k=1}^B \exp(\Phi(v_g^i, t_r^k)/\tau_3)} + \log \frac{\exp(\Phi(v_g^i, t_r^i)/\tau_3)}{\sum_{k=1}^B \exp(\Phi(v_g^k, t_r^i)/\tau_3)} \right) \quad (6)$$

AFLoc is trained to jointly optimize the local and global semantic alignment. The final loss function for AFLoc is:

$$L = L_{SW} + L_{DS} + L_{GR} \quad (7)$$

It is important to note that while concepts such as text encoding, image encoding, and multi-level semantic alignment have been explored in various studies, no research has demonstrated how to effectively design these concepts for annotation-free pathology localization. We drew inspiration from contrastive learning strategies such as ConVIRT, GLoRIA, and BioViL, and made effective extensions. By enhancing contrastive learning to focus not only on global image-text alignment but also on local semantic understanding, our approach significantly improves the capability for local pathology localization in annotation-free scenarios.

Inference. After the training, we transform the pathology localization task into a text-image matching problem by text prompts. Our model supports flexible text prompts that can be automatically generated using a simple template, such as ‘Findings suggesting {pathology}’, or adopt a detailed description of the pathology, like ‘Large right-sided pneumothorax, air space opacity in a right infrahilar location’. The input text is passed to the text encoder to obtain sentence-level features. For each input image, we use the image encoder to extract deep features, which are treated as local features. Next, we generate similarity maps that associate text prompts (pathology information) with images by calculating the similarity between text features and local image feature vectors. We then upscale the similarity maps to the original image size using bilinear interpolation and normalize them to the range [-1, 1], resulting in heatmaps for pathology localization. Applying a hard thresholding process to these heatmaps produces binarized segmentation masks.

For the classification task, we calculate the similarity between the global image features and the global features (report level) of both positive and negative text. Positive text can use the pathology localization prompts, while negative text can simply take the form ‘No {pathology}’. By calculating the softmax of the two similarities, we obtain the positive similarity as the probability of that pathology being positive.

Experimental details. For the MIMIC-CXR dataset, we preprocessed all chest X-ray images to a uniform size of 224×224 pixels and performed normalization. In our study, we focused on using a subset of the data that contains 249,262 frontal chest X-ray images and their corresponding textual descriptions. For the fundus image dataset, we adopted the same image preprocessing strategy as for MIMIC-CXR.

Typically, medical reports include ‘Findings’ and ‘Impressions’ sections. In our training data, we used the content of these two sections as training text to train our model. During training, we employed random shuffling and sentence sampling methods to further enhance the textual data. Moreover, for the fundus dataset, we performed additional sentence augmentation to increase the diversity of medical reports. Specifically, we performed

text augmentation on frequently occurring sentences in the reports, generating five semantically equivalent but differently expressed sentences for each sentence. During the training phase, these equivalent sentences were randomly replaced.

To train AFLoc, we used the Adam optimizer with an initial learning rate of 0.00002 and a momentum value of 0.9. Additionally, we implemented a learning rate decay mechanism, reducing the learning rate to 0.9 of its previous value after each epoch. All the hyperparameters, including batch size and learning rate, were optimized using the MIMIC-CXR validation dataset. The best model was obtained after training for 6 epochs with a batch size of 128.

Comparative Methods

In this section, we introduced the comparative algorithms we employed, which are categorized into four main groups: vision-language pre-training methods, self-supervised pre-training methods, unsupervised anomaly detection methods, and saliency-based methods. Each category will be discussed in detail in the following subsections.

Medical vision-language pre-training Methods. Four medical vision-language pre-training methods were compared in this study, including ConVIRT [49], GLoRIA [30], BioViL [28], and MedKLIP [19]. ConVIRT improves visual representations by maximizing the agreement between true image-text pairs versus random pairs via a bidirectional contrastive objective between the image and text modalities. GLoRIA proposes an attention-based framework that learns global and local representations by comparing subregions of images with words in paired reports. BioViL achieves better text modeling by adopting an improved lexicon and innovative language pre-training methods. Then, contrastive learning is utilized with paired text and images. MedKLIP first extracts medical information from radiology reports through a triplet extraction module. Then, it uses a Transformer-based fusion model to combine this information and visual signals at the image block level, enhancing the capability of medical diagnostics. These 4 methods were employed in our study as state-of-the-art medical vision-language pre-training comparative methods.

Self-supervised pre-training Methods. RETFound [13] is a self-supervised pre-training model for retinal images that learns generalizable representations from unlabeled retinal images, providing a basis for label-efficient model adaptation across various applications. In this study, we utilized this model for transfer learning on the retinal fundus dataset using classification annotations and compared it with our proposed annotations-free AFLoc.

Unsupervised Anomaly Detection Methods. This study compares ReContrast [24] and RD++ [23], two state-of-the-art unsupervised anomaly detection methods. ReContrast proposes a novel contrastive learning paradigm specifically designed for domain-specific unsupervised anomaly detection. This method enhances the transferability of the pre-trained encoder by jointly optimizing all parameters in an end-to-end fashion. The RD++ approach improves anomaly detection by increasing feature compactness and suppressing anomalous signals through a multi-task learning design. For the feature compactness task, RD++ introduces a self-supervised optimal transport method.

Saliency-based Methods. In addition to medical vision-language pre-training methods, 3 comparative saliency methods were also adopted in our study. Grad-CAM [15] uses the gradients flowing into the final convolutional layer for any target category to generate a coarse localization map, highlighting the important areas in the image used for classification. Grad-CAM++ [16] is an extension of Grad-CAM that aims to enhance and refine the visualization of the decision-making process of convolutional neural networks. Compared to the original Grad-CAM approach, Grad-CAM++ can provide clearer and more detailed visual explanations, especially in identifying specific classes in recognition models. Eigen-CAM [17] is a visualization technique to interpret the decisions of convolutional neural networks. It extends the traditional Class Activation Mapping (CAM) method, aiming to offer a more intuitive and detailed visual interpretation. The core idea of Eigen-CAM is to use principal component analysis to extract significant features from the outputs of the convolutional layers.

Acknowledgments

This research was partly supported by the National Natural Science Foundation of China (62222118, U22A2040), Shenzhen Science and Technology Program (RCYX20210706092-104034, JCYJ20220531100213029), Guangdong Provincial Key Laboratory of Artificial Intelligence in Medical Image Analysis and Application (2022B1212010011), the major key project of Peng Cheng Laboratory under grant PCL2023AS1-2, and Key Laboratory for Magnetic Resonance and Multimodality Imaging of Guangdong Province (2020B1212060051).

Data availability

MIMIC-CXR data is available at <https://physionet.org/content/mimic-cxr/2.0.0> for users with credentialed access. RSNA Pneumonia data is available at <https://www.rsna.org/rsnai/ai-image-challenge/> RSNA-Pneumonia-Detection-Challenge-2018. MS-CXR data is available at <https://physionet.org/content/ms-cxr/0.1/>. CheXlocalize data is available at <https://stanfordaimi.azurewebsites.net/datasets/abfb76e5-70d5-4315-badc-c94dd82e3d6d>. COVID Rural data is available at <https://www.cancerimagingarchive.net/collection/covid-19-ar/>. SIIM-ACR Pneumothorax data is available at <https://www.kaggle.com/c/siim-acr-pneumothorax-segmentation>. ChestX-Det10 data is available at <https://github.com/Deepwise-AILab/ChestX-Det10-Dataset>.

Code availability

The code is available on GitHub at <https://github.com/YH0517/AFLoc>.

References

- [1] Coudray, N. *et al.* Classification and mutation prediction from non-small cell lung cancer histopathology images using deep learning. *Nature medicine* **24**, 1559–1567 (2018).
- [2] Wang, P. *et al.* Development and validation of a deep-learning algorithm for the detection of polyps during colonoscopy. *Nature biomedical engineering* **2**, 741–748 (2018).
- [3] Campanella, G. *et al.* Clinical-grade computational pathology using weakly supervised deep learning on whole slide images. *Nature medicine* **25**, 1301–1309 (2019).
- [4] Courtiol, P. *et al.* Deep learning-based classification of mesothelioma improves prediction of patient outcome. *Nature medicine* **25**, 1519–1525 (2019).
- [5] Lee, S. Y. *et al.* Localization-adjusted diagnostic performance and assistance effect of a computer-aided detection system for pneumothorax and consolidation. *npj Digital Medicine* **5**, 107 (2022).
- [6] Cao, K. *et al.* Large-scale pancreatic cancer detection via non-contrast ct and deep learning. *Nature Medicine* 1–11 (2023).
- [7] Song, Z. *et al.* Clinically applicable histopathological diagnosis system for gastric cancer detection using deep learning. *Nature communications* **11**, 4294 (2020).
- [8] Leon, R. *et al.* Hyperspectral imaging benchmark based on machine learning for intraoperative brain tumour detection. *NPJ Precision Oncology* **7**, 119 (2023).
- [9] Rajpurkar, P., Chen, E., Banerjee, O. & Topol, E. J. Ai in health and medicine. *Nature medicine* **28**, 31–38 (2022).
- [10] Reed, C. J. *et al.* Self-supervised pretraining improves self-supervised pretraining. *Proceedings of the IEEE/CVF Winter Conference on Applications of Computer Vision* 2584–2594 (2022).
- [11] He, K., Fan, H., Wu, Y., Xie, S. & Girshick, R. Momentum contrast for unsupervised visual representation learning. *Proceedings of the IEEE/CVF conference on computer vision and pattern recognition* 9729–9738 (2020).
- [12] Chen, T., Kornblith, S., Norouzi, M. & Hinton, G. A simple framework for contrastive learning of visual representations. *International conference on machine learning* 1597–1607 (2020).
- [13] Zhou, Y. *et al.* A foundation model for generalizable disease detection from retinal images. *Nature* **622**, 156–163 (2023).
- [14] Saporta, A. *et al.* Benchmarking saliency methods for chest x-ray interpretation. *Nature Machine Intelligence* **4**, 867–878 (2022).

[15] Selvaraju, R. R. *et al.* Grad-cam: Visual explanations from deep networks via gradient-based localization. *2017 IEEE International Conference on Computer Vision (ICCV)* 618–626 (2017).

[16] Chattopadhyay, A., Sarkar, A., Howlader, P. & Balasubramanian, V. N. Grad-cam++: Generalized gradient-based visual explanations for deep convolutional networks. *2018 IEEE Winter Conference on Applications of Computer Vision (WACV)* 839–847 (2018).

[17] Muhammad, M. B. & Yeasin, M. Eigen-cam: Class activation map using principal components. *2020 international joint conference on neural networks (IJCNN)* 1–7 (2020).

[18] Tiu, E. *et al.* Expert-level detection of pathologies from unannotated chest x-ray images via self-supervised learning. *Nature Biomedical Engineering* **6**, 1399–1406 (2022).

[19] Wu, C., Zhang, X., Zhang, Y., Wang, Y. & Xie, W. Medklip: Medical knowledge enhanced language-image pre-training. *Proceedings of the IEEE/CVF International Conference on Computer Vision* (2023).

[20] Morens, D. M. & Fauci, A. S. Emerging infectious diseases: threats to human health and global stability. *PLoS pathogens* **9**, e1003467 (2013).

[21] Baur, C., Denner, S., Wiestler, B., Navab, N. & Albarqouni, S. Autoencoders for unsupervised anomaly segmentation in brain mr images: A comparative study. *Medical Image Analysis* 101952 (2021).

[22] Deng, H. & Li, X. Anomaly detection via reverse distillation from one-class embedding. *2022 IEEE/CVF Conference on Computer Vision and Pattern Recognition* 9727–9736 (2022).

[23] Tien, T. D. *et al.* Revisiting reverse distillation for anomaly detection. *Proceedings of the IEEE/CVF Conference on Computer Vision and Pattern Recognition* 24511–24520 (2023).

[24] Guo, J., lu, s., Jia, L., Zhang, W. & Li, H. Recontrast: Domain-specific anomaly detection via contrastive reconstruction. *Advances in Neural Information Processing Systems* **36**, 10721–10740 (2023).

[25] Lagogiannis, I., Meissen, F., Kaassis, G. & Rueckert, D. Unsupervised pathology detection: A deep dive into the state of the art. *IEEE Transactions on Medical Imaging* **43**, 241–252 (2024).

[26] Yan, B. & Pei, M. Clinical-bert: Vision-language pre-training for radiograph diagnosis and reports generation. *Proceedings of the AAAI Conference on Artificial Intelligence* **36**, 2982–2990 (2022).

[27] Bannur, S. *et al.* Learning to exploit temporal structure for biomedical vision-language processing. *Proceedings of the IEEE/CVF Conference on Computer Vision and Pattern Recognition* 15016–15027 (2023).

[28] Boecking, B. *et al.* Making the most of text semantics to improve biomedical vision–language processing. *European conference on computer vision* 1–21 (2022).

[29] Zhang, Y., Jiang, H., Miura, Y., Manning, C. D. & Langlotz, C. P. Contrastive learning of medical visual representations from paired images and text. *Machine Learning for Healthcare Conference* 2–25 (2022).

[30] Huang, S.-C., Shen, L., Lungren, M. P. & Yeung, S. Gloria: A multimodal global-local representation learning framework for label-efficient medical image recognition. *Proceedings of the IEEE/CVF International Conference on Computer Vision* 3942–3951 (2021).

[31] Zhou, H.-Y., Lian, C., Wang, L. & Yu, Y. Advancing radiograph representation learning with masked record modeling. *The Eleventh International Conference on Learning Representations* (2023).

[32] Johnson, A. E. *et al.* Mimic-cxr, a de-identified publicly available database of chest radiographs with free-text reports. *Scientific data* **6**, 317 (2019).

[33] Shih, G. *et al.* Augmenting the national institutes of health chest radiograph dataset with expert annotations of possible pneumonia. *Radiology: Artificial Intelligence* **1**, e180041 (2019).

[34] Desai, S. *et al.* Chest imaging representing a covid-19 positive rural us population. *Scientific data* **7**, 414 (2020).

[35] Tang, H., Sun, N., Li, Y. & Xia, H. Deep learning segmentation model for automated detection of the opacity regions in the chest x-rays of the covid-19 positive patients and the application for disease severity. *medRxiv* 2020–10 (2020).

[36] Liu, J., Lian, J. & Yu, Y. Chestx-det10: Chest x-ray dataset on detection of thoracic abnormalities (2020). 2006.10550v3.

[37] Anna, Z. *et al.* Siim-acr pneumothorax segmentation (2019). URL <https://kaggle.com/competitions/siim-acr-pneumothorax-segmentation>.

[38] Reed, J. C. Multifocal ill-defined opacities. *Chest Radiology* 243 (2011).

[39] Woodring, J. H. & Reed, J. C. Types and mechanisms of pulmonary atelectasis. *Journal of thoracic imaging* **11**, 92–108 (1996).

[40] Lim, L. S., Mitchell, P., Seddon, J. M., Holz, F. G. & Wong, T. Y. Age-related macular degeneration. *The Lancet* **379**, 1728–1738 (2012).

[41] Uhler, T. A. & Piltz-Seymour, J. Optic disc hemorrhages in glaucoma and ocular hypertension: implications and recommendations. *Current Opinion in Ophthalmology* **19**, 89–94 (2008).

[42] Rezatofighi, H. *et al.* Generalized intersection over union: A metric and a loss for bounding box regression. *Proceedings of the IEEE/CVF conference on computer vision and pattern recognition* 658–666 (2019).

[43] Franquet, T. Imaging of community-acquired pneumonia. *Journal of thoracic imaging* **33**, 282–294 (2018).

[44] Li, C. *et al.* LLaVA-med: Training a large language-and-vision assistant for biomedicine in one day (2023). URL <https://openreview.net/forum?id=GSuP99u2kR>.

[45] Alsentzer, E. *et al.* Publicly available clinical bert embeddings. *NAACL HLT 2019* 72 (2019).

[46] Peng, Y., Yan, S. & Lu, Z. Transfer learning in biomedical natural language processing: An evaluation of bert and elmo on ten benchmarking datasets (2019).

[47] Li, Z. *et al.* Thoracic disease identification and localization with limited supervision 8290–8299 (2018).

[48] He, K., Zhang, X., Ren, S. & Sun, J. Deep residual learning for image recognition. *Proceedings of the IEEE conference on computer vision and pattern recognition* 770–778 (2016).

[49] Zhang, Y., Jiang, H., Miura, Y., Manning, C. D. & Langlotz, C. P. Contrastive learning of medical visual representations from paired images and text 2–25 (2022).

Appendix A

Extended Data Table 1: Quantitative pathology localization results of different models on the 3 chest x-ray datasets: RSNA Pneumonia, COVID Rural, MS-CXR. Numbers within parentheses indicate 95% CI.

Methods	RSNA Pneumonia	Covid-Rural	MS-CXR
IoU			
ReContrast	0.054 (0.050, 0.058)	0.027 (0.020, 0.035)	0.087 (0.072, 0.102)
RD++	0.050 (0.047, 0.054)	0.058 (0.046, 0.072)	0.090 (0.075, 0.105)
GLoRIA	0.278 (0.269, 0.286)	0.138 (0.119, 0.159)	0.268 (0.242, 0.295)
BioViL	0.295 (0.286, 304)	0.191 (0.170, 0.215)	0.228 (0.201, 0.255)
MedKLIP	0.317 (0.309, 0.325)	0.174 (0.156, 0.192)	0.264 (0.240, 0.288)
AFLoc	0.342 (0.332, 0.350)	0.211 (0.185, 0.236)	0.324 (0.298, 0.350)
Dice			
ReContrast	0.095 (0.089, 0.10)	0.049 (0.037, 0.06)	0.148 (0.125, 0.171)
RD++	0.087 (0.081, 0.093)	0.100 (0.081, 0.119)	0.152 (0.130, 0.176)
GLoRIA	0.411 (0.400, 0.421)	0.223 (0.193, 0.251)	0.392 (0.357, 0.427)
BioViL	0.433 (0.423, 0.443)	0.298 (0.268, 0.329)	0.342 (0.308, 0.377)
MedKLIP	0.465 (0.455, 0.474)	0.281 (0.252, 0.308)	0.394 (0.365, 0.423)
AFLoc	0.484 (0.474, 0.495)	0.323 (0.289, 0.355)	0.462 (0.431, 0.492)
CNR			
ReContrast	0.087 (0.064, 0.109)	-0.244 (-0.325, -0.165)	0.465 (0.398, 0.530)
RD++	0.225 (0.201, 0.248)	0.289 (0.214, 0.361)	0.539 (0.474, 0.602)
GLoRIA	1.223 (1.176, 1.272)	0.663 (0.560, 0.770)	1.287 (1.149, 1.421)
BioViL	1.300 (1.262, 1.339)	0.975 (0.880, 1.065)	1.083 (0.949, 1.219)
MedKLIP	1.032 (1.014, 1.051)	0.838 (0.772, 0.906)	1.044 (0.959, 1.132)
AFLoc	1.538 (1.496, 1.580)	1.062 (0.929, 1.173)	1.636 (1.501, 1.772)

Extended Data Table 2: Quantitative results (IoU) of different models for different pathologies on the MS-CXR dataset. Numbers within parentheses indicate 95% CI.

Method	Pneumonia	Atelectasis	Consolidation	Pneumothorax	Pleural Effusion	Lung Opacity	Cardiomegaly	Edema
ReContrast	0.090	0.079	0.098	0.053	0.061	0.061	0.131	0.120
	(0.080, 0.100)	(0.064, 0.095)	(0.082, 0.115)	(0.045, 0.062)	(0.048, 0.074)	(0.046, 0.078)	(0.121, 0.140)	(0.092, 0.150)
	0.093	0.075	0.120	0.093	0.048	0.078	0.073	0.162
RD++	(0.084, 0.103)	(0.063, 0.088)	(0.101, 0.139)	(0.084, 0.103)	(0.037, 0.058)	(0.060, 0.098)	(0.066, 0.080)	(0.129, 0.193)
	0.290	0.303	0.304	0.116	0.330	0.196	0.408	0.201
	(0.265, 0.314)	(0.266, 0.339)	(0.277, 0.330)	(0.099, 0.133)	(0.304, 0.357)	(0.164, 0.230)	(0.398, 0.420)	(0.165, 0.236)
GLoRIA	0.305	0.266	0.299	0.109	0.227	0.178	0.267	0.171
	(0.284, 0.328)	(0.222, 0.312)	(0.273, 0.325)	(0.094, 0.124)	(0.205, 0.250)	(0.148, 0.209)	(0.247, 0.286)	(0.135, 0.206)
	0.296	0.324	0.265	0.092	0.216	0.197	0.394	0.326
MedKLIP	(0.277, 0.315)	(0.294, 0.355)	(0.238, 0.289)	(0.078, 0.106)	(0.195, 0.237)	(0.167, 0.228)	(0.384, 0.404)	(0.285, 0.366)
	0.412	0.381	0.371	0.117	0.350	0.327	0.367	0.269
	(0.386, 0.435)	(0.344, 0.417)	(0.345, 0.395)	(0.099, 0.135)	(0.326, 0.375)	(0.290, 0.364)	(0.357, 0.377)	(0.237, 0.299)

Extended Data Table 3: Quantitative results (IoU) from the ablation study to investigate the importance of aligning image features with text features at different levels.

Different Levels of Features			RSNA Pneumonia	COVID Rural	MS-CXR	CheXlocalize	Mean
Word – Shallow local	Sentence – Deep local	Report – Global					
✓			0.239	0.147	0.180	0.133	0.175
	✓		0.281	0.169	0.318	0.301	0.267
		✓	0.191	0.056	0.105	0.186	0.135
✓	✓		0.329	0.177	0.264	0.285	0.264
✓		✓	0.254	0.159	0.175	0.200	0.197
	✓	✓	0.285	0.211	0.325	0.305	0.282
✓	✓	✓	0.342	0.212	0.324	0.318	0.299

Extended Data Table 4: Quantitative results of different models on the retinal fundus dataset. Numbers within parentheses indicate 95% CI.

Methods	Choroidal neovascularization	Drusen	Intraretinal hemorrhage	Mean
IoU				
ReContrast	0.080 (0.068, 0.093)	0.027 (0.019, 0.035)	0.035 (0.031, 0.038)	0.047 (0.039, 0.055)
RD++	0.121 (0.112, 0.131)	0.062 (0.051, 0.077)	0.051 (0.047, 0.054)	0.078 (0.070, 0.087)
ConVIRT	0.131 (0.119, 0.144)	0.120 (0.099, 0.140)	0.079 (0.074, 0.085)	0.110 (0.097, 0.123)
GLoRIA	0.143 (0.130, 0.156)	0.107 (0.085, 0.128)	0.075 (0.070, 0.080)	0.108 (0.095, 0.121)
AFLoc	0.321 (0.303, 0.337)	0.147 (0.125, 0.170)	0.097 (0.091, 0.102)	0.188 (0.173, 0.203)
Dice				
ReContrast	0.124 (0.107, 0.141)	0.046 (0.034, 0.061)	0.064 (0.058, 0.069)	0.078 (0.066, 0.090)
RD++	0.194 (0.179, 0.209)	0.105 (0.087, 0.124)	0.092 (0.087, 0.098)	0.130 (0.118, 0.144)
ConVIRT	0.205 (0.187, 0.223)	0.187 (0.156, 0.215)	0.141 (0.132, 0.149)	0.178 (0.158, 0.199)
GLoRIA	0.224 (0.205, 0.242)	0.168 (0.137, 0.197)	0.134 (0.126, 0.142)	0.175 (0.156, 0.194)
AFLoc	0.451 (0.430, 0.470)	0.225 (0.192, 0.257)	0.170 (0.160, 0.178)	0.282 (0.261, 0.302)
CNR				
ReContrast	0.901 (0.850, 0.954)	0.421 (0.329, 0.510)	0.253 (0.231, 0.274)	0.525 (0.470, 0.579)
RD++	0.673 (0.635, 0.707)	0.457 (0.395, 0.521)	0.210 (0.191, 0.229)	0.447 (0.407, 0.486)
ConVIRT	0.359 (0.278, 0.447)	0.652 (0.517, 0.778)	0.255 (0.231, 0.278)	0.422 (0.342, 0.501)
GLoRIA	0.493 (0.427, 0.563)	0.655 (0.512, 0.787)	0.216 (0.194, 0.237)	0.455 (0.378, 0.529)
AFLoc	1.452 (1.368, 1.534)	0.925 (0.783, 1.063)	0.372 (0.349, 0.396)	0.916 (0.833, 0.998)

Extended Data Table 5: Quantitative results (IoU) of different models for different pathologies on the CheXlocalize dataset. *Results obtained from CheXlocalize [14].

Method	Airspace opacity	Atelectasis	Edema	Consolidation	Pleural effusion	Cardiomegaly	Enlarged cardio	Lung lesion	Pneumothorax	Support devices
Grad-CAM*	0.248	0.254	0.362	0.408	0.235	0.452	0.379	0.101	0.213	0.163
Grad-CAM++*	0.234	0.245	0.388	0.296	0.195	0.346	0.400	0.089	0.216	0.133
Eigen-CAM*	0.293	0.267	0.370	0.332	0.249	0.379	0.372	0.089	0.218	0.116
AFLoc	0.293	0.367	0.431	0.348	0.248	0.485	0.460	0.185	0.175	0.184
Human benchmark*	0.260	0.124	0.335	0.179	0.219	0.720	0.569	0.426	0.435	0.444

Extended Data Table 6: Quantitative results (IoU) of the proposed AFLoc model at different thresholds for eight pathologies in the MS-CXR dataset. The model demonstrates relatively stable localization performance across various pathologies at multiple thresholds. Numbers within parentheses indicate 95% CI.

Threshold	Pneumonia	Atelectasis	Consolidation	Pneumothorax	Pleural Effusion	Lung Opacity	Cardiomegaly	Edema
0.1	0.419 (0.393, 0.444)	0.391 (0.350, 0.428)	0.378 (0.350, 0.406)	0.129 (0.109, 0.149)	0.334 (0.306, 0.361)	0.295 (0.256, 0.339)	0.453 (0.441, 0.464)	0.305 (0.262, 0.348)
0.2	0.429 (0.402, 0.455)	0.400 (0.357, 0.441)	0.383 (0.355, 0.411)	0.125 (0.105, 0.145)	0.351 (0.326, 0.376)	0.316 (0.274, 0.355)	0.416 (0.405, 0.428)	0.288 (0.252, 0.320)
0.3	0.428 (0.401, 0.454)	0.397 (0.357, 0.441)	0.381 (0.353, 0.407)	0.119 (0.101, 0.140)	0.361 (0.336, 0.385)	0.333 (0.295, 0.371)	0.372 (0.362, 0.382)	0.269 (0.235, 0.301)
0.4	0.410 (0.382, 0.436)	0.375 (0.335, 0.416)	0.367 (0.340, 0.393)	0.112 (0.094, 0.132)	0.359 (0.331, 0.386)	0.345 (0.308, 0.381)	0.323 (0.313, 0.333)	0.254 (0.214, 0.291)
0.5	0.373 (0.348, 0.399)	0.339 (0.299, 0.379)	0.343 (0.315, 0.372)	0.101 (0.083, 0.119)	0.345 (0.314, 0.376)	0.345 (0.307, 0.383)	0.270 (0.261, 0.279)	0.231 (0.190, 0.271)

Extended Data Table 7: Quantitative results from replacing different text encoders in the MS-CXR dataset to investigate their impact on localization outcomes.

Text encoder	IoU	Dice	CNR
llava-med-v1.5-mistral-7b	0.307	0.441	1.483
BioClinicalBERT	0.324	0.461	1.634